

Elliptic Dichroism and Valley-Selective Optical Pumping in the Surface of Topological Crystalline Insulator

Motohiko Ezawa

Department of Applied Physics, University of Tokyo, Hongo 7-3-1, 113-8656, Japan

The low-energy theory of the surface of the topological crystalline insulator (TCI) is described by four Dirac fermions with different velocities into the x and y directions. The TCI surface provides us with a new way to valleytronics. We investigate the optical absorption in the TCI surface. It shows a strong elliptic dichroism, which is characterized by a selection rule between the right and left elliptic polarized lights owing to the anisotropy of the Dirac cone though the four Dirac fermions have the same chiralities. We can selectively excite electrons on specific valleys by adjusting the ellipticity of the light with the anisotropy of the Dirac fermion. By measuring this elliptic dichroism, it is also possible to determine the anisotropy of a Dirac cone experimentally.

I. INTRODUCTION

Valleytronics is a promising candidate of the next generation electronics¹⁻⁴. It is a technology of manipulating the degree of freedom to which inequivalent degenerate state an electron belongs near the Fermi level. The main target of valleytronics is the honeycomb system. Indeed, the honeycomb structure is an ideal play ground of valleytronics since it has two inequivalent Dirac cones or *valleys*. A key progress in valleytronics is valley-selective optical pumping⁴⁻⁸. By applying circular polarized light in a gapped Dirac system, we can selectively excite electrons in one valley based on the property that two valleys have opposite chiralities. It is known as the circular dichroism. Valley-selective pumping has been observed⁹⁻¹⁴ in the transition-metal dichalcogenides such as MoS₂, where there exists a direct gap between the conduction and valence bands for Dirac fermions.

However, the valleytronics is not restricted to the honeycomb system. Recently, the topological crystalline insulator (TCI) attracts much attention due to its experimental realizations¹⁵⁻¹⁷ in Pb_{1-x}Sn_xTe. It is a topological insulator protected by the mirror symmetry^{18,19}. The remarkable properties of the TCI is that there emerge four topological protected surface Dirac cones, as has been observed in the ARPES experiment¹⁵⁻¹⁷. The appearance of several topologically protected Dirac cones enables us to use the TCI as the basic material for the valleytronics. Recent experiments²⁰ show that the band gap can be introduced in the surface Dirac cones by crystal distortion by applying strain to the crystal structure.

In this paper, we investigate the optical absorption of the TCI surface. The key properties of surface Dirac cones are that all of them have the same chirality but that each of them has a particular anisotropy. Based on the anisotropy, we can selectively excite electrons in different valley by the elliptically polarized light. This is a new type of dichroism different from the circular dichroism. We call it an *elliptic dichroism*. We propose an experimental method to determine the anisotropy of the velocities and the band gap of Dirac cones with the use of elliptic dichroism. Our finding will open a new way of the valleytronics based on the TCI.

II. HAMILTONIAN

Recent ARPES experiments¹⁵⁻¹⁷ show that there are four Dirac cones at $\Lambda_X, \Lambda'_X, \Lambda_Y$ and Λ'_Y points in the [001] surface state of the TCI, whose band structure we show in Fig.1. They may be used as the valley degree of freedom. Two Dirac cones are present at the Λ_X and Λ'_X points near the X point but slightly away from the X point along the x axis in the momentum space. The other two Dirac cones are present at the Λ_Y and Λ'_Y points near the Y point along the y axis.

The Hamiltonian for the [001] surface states of the TCI near the X point is given by²¹⁻²⁴

$$H_X(\mathbf{k}) = v_1 k_x \sigma_y - v_2 k_y \sigma_x + n \tau_x + n' \sigma_y \tau_y + m \sigma_z, \quad (1)$$

where σ and τ are the Pauli matrixes for the spin and the pseudospin representing the cation-anion degree of freedom, respectively: n and n' describe the pseudospin mixing. We have set $\hbar = 1$ for simplicity. This Hamiltonian describes PbTe for $n > 0$ and SnTe for $n < 0$. We can continuously change the value n by choosing the chemical interpolating materials Pb_{1-x}Sn_xTe. Typical values are $v_1 = 1.3\text{eV}$, $v_2 = 2.4\text{eV}$, $n = 70\text{meV}$ and $n' = 26\text{meV}$. We have added the mass term $m \sigma_z$, which will be introduced by strain and magnetization^{19,25}. The mass acquisition by crystal distortion has been observed in recent experiments²⁰. It is possible to change the mass term independently in four Dirac cones by applying the strain to the crystal^{20,25}. The mass term is necessary for the valley-selective optical absorption to occur. However the following analysis is independent of detailed origins of the mass term.

The corresponding Hamiltonian near the Y point is given by

$$H_Y(\mathbf{k}) = v_2 k_x \sigma_y - v_1 k_y \sigma_x + n \tau_x + n' \sigma_x \tau_y + m \sigma_z. \quad (2)$$

Note that the velocities into the x and y directions are different at the Y point from those at the X point, as is a manifestation of the four-fold rotation symmetry.

It follows from (1) that the energy spectrum is given by

$$E(\mathbf{k}) = \pm \sqrt{f \pm 2\sqrt{g}} \quad (3)$$

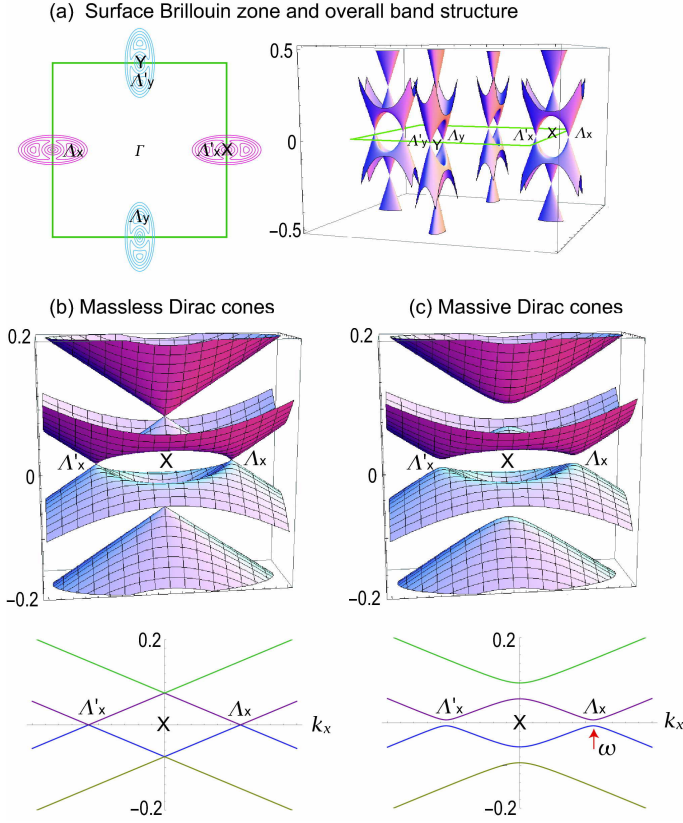


FIG. 1: (Color online) (a) Surface Brillouin zone centered at the Γ point and bounded by the X and Y points. There are low-energy Dirac cones at the $\Lambda_X, \Lambda'_X, \Lambda_Y, \Lambda'_Y$ points, and high-energy Dirac cones at the X and Y points. (b) Detailed band structure in the vicinity of the X point. Two low-energy Dirac cones are formed at the Λ_X and Λ'_X points. (c) The gaps open when the mass term is present.

in the vicinity of the X point with

$$f = n^2 + n'^2 + v_1^2 k_x^2 + v_2^2 k_y^2 + m^2, \quad (4)$$

$$g = (n^2 + n'^2)v_1^2 k_x^2 + n^2 v_2^2 k_y^2 + n^2 m^2. \quad (5)$$

We show the band structure in Fig.1. The gap closes at the two points $(k_x, k_y) = (\pm\Lambda, 0)$ with $\Lambda = \sqrt{n^2 + n'^2}/v_1$ without the mass term ($m = 0$).

By linearizing the band structure around the Λ_X point, we obtain the two-component low-energy Hamiltonian for massless Dirac fermions^{21,23},

$$H_{\Lambda_X}(\tilde{\mathbf{k}}) = v_1 \tilde{k}_x \sigma_y - \tilde{v}_2 \tilde{k}_y \sigma_x + \tilde{m} \sigma_z, \quad (6)$$

where $\tilde{k}_x = k_x \mp \Lambda$ and $\tilde{k}_y = k_y$, with the renormalized velocity,

$$\tilde{v}_2 = v_2 n' / \sqrt{n^2 + n'^2} = 0.84 \text{eV}, \quad (7)$$

and the renormalized mass,

$$\tilde{m} = \sqrt{m^2 + 2n^2 + 2n'^2 - 2\sqrt{(n^2 + n'^2)^2 + m^2 n^2}}. \quad (8)$$

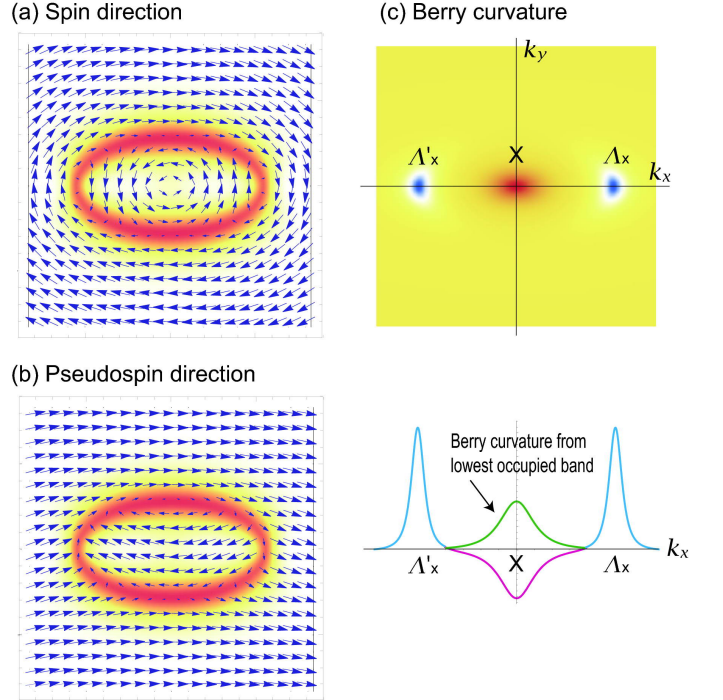


FIG. 2: (Color online) (a) Spin direction of the TCI surface in the vicinity of the X point. The oval (red) indicates the region where the magnitude of spin is quite small. The spin directions are opposite inside and outside the oval. The spin rotation is clockwise (anticlockwise) in the low-energy (high-energy) Dirac cones at the Λ_X and Λ'_X points (the X point). (b) Pseudospin direction of the TCI surface in the vicinity of the X point. The oval (red) indicates the region where the magnitude of pseudospin is quite small. The pseudospin directions are opposite inside and outside the oval. (c) Berry curvature of the highest occupied band. It has a sharp peak (red) at the X point and sharp peaks (blue) at the Λ_X and Λ'_X points. The Chern number contribution from the Berry curvature at the X point is exactly cancelled out by the one (green) from the Dirac cone in the lowest occupied band at the X point.

The energy spectrum reads

$$E_{\Lambda_X} = \pm \sqrt{v_1^2 \tilde{k}_x^2 + \tilde{v}_2^2 \tilde{k}_y^2 + \tilde{m}^2}. \quad (9)$$

The linearized Hamiltonian around the Λ'_X point has precisely the same expression as (6). Hence we call it the one around the Λ_X (Λ'_X) point. In the same way we have the low-energy Hamiltonian around the Λ_Y (Λ'_Y) point,

$$H_{\Lambda_Y}(\tilde{\mathbf{k}}) = \tilde{v}_2 \tilde{k}_x \sigma_y - v_1 \tilde{k}_y \sigma_x + \tilde{m} \sigma_z, \quad (10)$$

where $\tilde{k}_x = k_x$ and $\tilde{k}_y = k_y \mp \Lambda$. We make comments on the Dirac Hamiltonians (6) and (10). First, the chiralities of all four Dirac cones are identical at the Λ_X (Λ'_X) and Λ_Y (Λ'_Y) points, which can be verified by studying the spin direction. Nevertheless, it is possible to make a selective excitation between the Λ_X (Λ'_X) point and the Λ_Y (Λ'_Y) point, because the Dirac cones are anisotropic, where $\tilde{v}_2/v_1 = 0.84$. Namely, this anisotropy leads to an experimentally observable effect, that is the elliptic dichroism.

III. SPIN DIRECTION AND BERRY PHASE

We illustrate the expectation value of the spin $\langle \mathbf{s} \rangle = \langle \psi | \mathbf{s} | \psi \rangle$ in the vicinity of the X point in Fig.2(a). There is one up-pointing vortex with anti-clockwise vorticity at the X point, and there are two down-pointing vortices with clockwise vorticity at the Λ_X and Λ'_X points^{24,26,27}. They describe the spin directions of electrons in one Dirac cone at the X point, and two Dirac cones at the Λ_X and Λ'_X points in Fig.1.

This structure is understood as follows. Let us assume $n = 0$ and $n' = 0$ in the Hamiltonian (1). Then the two Dirac cones in the conduction and valence bands touch each other at the Fermi level. The effect of the term $n\tau_x$ is to shift these Dirac cones to intersect one another, forming an intersection oval. (It is an oval and not a circle since $v_1 \neq v_2$.) These two Dirac cones have opposite chiralities, which leads to the opposite spin rotations inside and outside the oval. We now switch on n' . Then the level crossing turns into the level anticrossing with the resulting band structure as in Fig.1(a), where Dirac cones emerge at the Λ_X and Λ'_X points. The spin rotates around each Dirac cone. The magnitude of spin, $s^2 = s_x^2 + s_y^2 + s_z^2$, is found to be quite small around the oval [Fig.2(a)]. We clearly see the directions of the spin rotation are identical in the four valleys at Λ_X , Λ'_X , Λ_Y and Λ'_Y , which manifests the identical chirality of the four low-energy Dirac cones. On the other hand, the spin rotation in the two high-energy Dirac cones at the X and Y points is opposite to the one in the low-energy Dirac cones. The spin direction has been observed by means of spin-resolved ARPES¹⁶ and spin-resolved photoelectron spectroscopy (SRPES)²⁶.

We have also illustrated the expectation value of the pseudospin in the vicinity of the X point in Fig.2(b). The pseudospin vector points the x -direction when $n' = 0$ in the Hamiltonian (1), since then τ_x is a good quantum number. The pseudospin direction is inverted at the oval, which is the intersection of the two Dirac cones. When $n' \neq 0$, the magnitude of the pseudospin, $\mathbf{t}^2 = t_x^2 + t_y^2 + t_z^2$, becomes quite small also around the oval. Needless to say the magnitude of the SU(4) spin is the same everywhere. It indicates that the spin-pseudospin entanglement becomes largest around the oval.

We illustrate the Berry curvature $F(\mathbf{k})$ of the highest unoccupied state in Fig.2(c). The Berry curvature exhibits sharp peaks at the vortex centers of the spin rotation, which correspond to the tips of the Dirac cones. Note that the Berry curvature at the X point is exactly canceled out by the one from the other occupied band, and does not contribute to the Chern number. In the vicinity of the Λ_X and Λ'_X points, we obtain an analytic form for the Berry curvature $F(\mathbf{k})$ by using the low-energy Hamiltonian (6),

$$F(\mathbf{k}) = \frac{\tilde{m}v_1\tilde{v}_2}{(v_1^2k_x^2 + \tilde{v}_2^2k_y^2 + \tilde{m}^2)^{3/2}}. \quad (11)$$

The Chern number is explicitly calculated as

$$\mathcal{C} = \frac{1}{2\pi} \int F(\mathbf{k}) d\mathbf{k} = \frac{1}{2} \text{sgn}(\tilde{m}) \quad (12)$$

for each cone. The total Chern number is ± 2 since there are four Dirac cones contributing equally to the Chern number. By applying strain to the crystal, we can induce different mass terms in four Dirac cones. Then the total Chern number takes values 2, 1, 0, -1 , -2 depending on the sign of the four mass terms.

IV. OPTICAL ABSORPTION AND ELLIPTIC DICHROISM

An interesting experiment to probe and manipulate the valley degree of freedom is to employ the optical absorption⁴⁻⁷. It is possible to excite massive Dirac electrons by the right or left circularly polarized light, known as circular dichroism. Originally, circular dichroism is proposed in honeycomb systems where the velocities of the Dirac cones are isotropic. On the other hand they are anisotropic in the TCI surface. This leads to the elliptic dichroism, where the optical absorptions are very different between the right and left elliptically polarized lights.

We explore optical inter-band transitions from the state $|u_v(\tilde{\mathbf{k}})\rangle$ in the valence band to the state $|u_c(\tilde{\mathbf{k}})\rangle$ in the conduction band. The fundamental transition is a transition from the highest occupied band to the lowest unoccupied band (Fig.1). We inject a beam of elliptical polarized light onto the TCI surface. The corresponding electromagnetic potential is given by $\mathbf{A}(t) = (A_x \sin \omega t, A_y \cos \omega t)$. The electromagnetic potential is introduced into the Hamiltonian by way of the minimal substitution, that is, by replacing the momentum \tilde{k}_i with the covariant momentum $P_i \equiv \tilde{k}_i + eA_i$. The resultant Hamiltonian simply reads $H(A) = H + \mathcal{P}_x A_x + \mathcal{P}_y A_y$, with

$$\mathcal{P}_x = \frac{\partial H}{\partial \tilde{k}_x}, \quad \mathcal{P}_y = \frac{\partial H}{\partial \tilde{k}_y}, \quad (13)$$

in the linear response theory. The optical matrix element between the initial and final states in the photo-emission process is given by⁴⁻⁷

$$P_i(\tilde{\mathbf{k}}) \equiv m_0 \langle u_c(\tilde{\mathbf{k}}) | \frac{\partial H}{\partial \tilde{k}_i} | u_v(\tilde{\mathbf{k}}) \rangle. \quad (14)$$

We define the optical matrix element of the elliptic polarization for the right (+) and left (-) polarized lights,

$$P_\theta^\pm(\tilde{\mathbf{k}}) = P_x(\tilde{\mathbf{k}}) \cos \theta \pm i P_y(\tilde{\mathbf{k}}) \sin \theta, \quad (15)$$

where θ is the ellipticity of the injected beam.

The wave functions $|u_v(\tilde{\mathbf{k}})\rangle$ and $|u_c(\tilde{\mathbf{k}})\rangle$ are obtained explicitly by diagonalizing the Hamiltonian (1). It is possible to derive an explicit form of $|P_\theta^\pm(\tilde{\mathbf{k}})|^2$ at the Λ_X and Λ'_X points for arbitrary ellipticity θ ,

$$\lim_{\tilde{\mathbf{k}} \rightarrow 0} |P_\theta^\pm(\tilde{\mathbf{k}})|^2 = (v_1 \cos \theta \pm \text{sgn}[\tilde{m}] \tilde{v}_2 \sin \theta)^2. \quad (16)$$

We show the ellipticity dependence of the optical matrix element (16) in Fig.3(a). It is remarkable that the system shows a perfect elliptic dichroism when $\theta = \theta_1$ with

$$\theta_1 = \arctan(v_1/\tilde{v}_2), \quad (17)$$

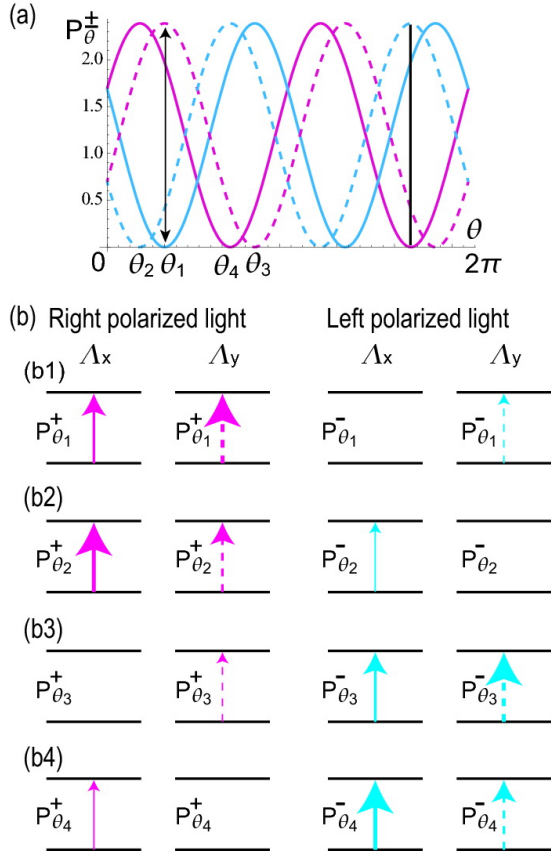


FIG. 3: (Color online) (a) Optical matrix element $|P_{\theta}^{\pm}|$ at the Λ_X and Λ_Y points with various ellipticity θ [eq.(16)]. Solid (dotted) curves are optical absorption at X (Y) point, and red (blue) curves are for $|P_{\theta}^+|$ ($|P_{\theta}^-|$). (b) Illustration of optical absorption when (b1) $\theta = \theta_1$, (b2) $\theta = \theta_2$, (b3) $\theta = \theta_3$, (b4) $\theta = \theta_4$. The magnitude of arrows indicates the magnitude of optical absorption.

where

$$\lim_{\tilde{\mathbf{k}} \rightarrow 0} |P_{\theta_1}^{\pm}(\tilde{\mathbf{k}})|^2 = m_0^2 v_1 \tilde{v}_2 (1 \pm \text{sgn}[\tilde{m}])^2. \quad (18)$$

Indeed, it follows that $|P_{\theta_1}^-(0)|^2 = 0$ if $\tilde{m} > 0$, while $|P_{\theta_1}^+(0)|^2 = 0$ if $\tilde{m} < 0$. On the other hand, if $\tilde{m} = 0$, the system does not show a significant dichroism. Substituting the values $v_1 = 1.3\text{eV}$ and $\tilde{v}_2 = 0.84\text{eV}$, we obtain $\theta_1 = 0.318\pi$.

In the same way, we find the optical matrix element at the Y point,

$$\lim_{\tilde{\mathbf{k}} \rightarrow 0} |P_{\theta}^{\pm}(\tilde{\mathbf{k}})|^2 = (\tilde{v}_2 \cos \theta \pm \text{sgn}[\tilde{m}] v_1 \sin \theta)^2. \quad (19)$$

We show the ellipticity dependence of the optical absorption (19) at the Y point in Fig.3(a) by dotted curves. The condition for the perfect elliptic dichroism is changed to be

$$\theta_2 = \arctan(\tilde{v}_2/v_1), \quad (20)$$

which yields $\theta_2 = 0.182\pi$.

There are two additional critical angles of the perfect elliptical dichroism. Noting that substituting $\theta \mapsto \theta + \pi/2$, (16)

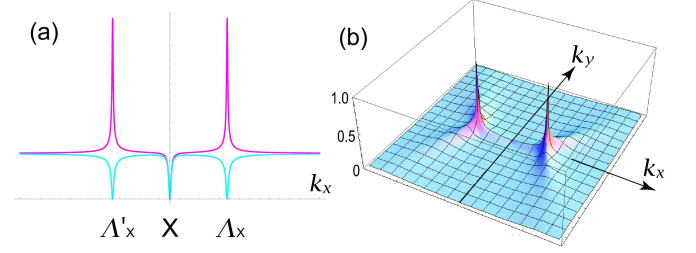


FIG. 4: (Color online) (a) Optical matrix element $|P_{\theta_c}^+(\tilde{\mathbf{k}})|^2$ (red curve) and $|P_{\theta_c}^-(\tilde{\mathbf{k}})|^2$ (blue curve) along the \tilde{k}_x axis, (b) $\tilde{\mathbf{k}}$ -resolved optical polarization $\eta(\tilde{\mathbf{k}})$. It has two sharp peaks at Λ_X and Λ'_X points. We have taken $\tilde{m} = 2\text{meV}$.

and (19) interchange. Thus we have $\theta_3 = \theta_1 + \pi/2 = 0.818\pi$ and $\theta_4 = \theta_2 + \pi/2 = 0.682\pi$.

The imaginary part of the dielectric function arises due to inter-band absorption, and is given by

$$\begin{aligned} \varepsilon_{\pm}(\omega) = & \frac{\pi e^2}{\varepsilon_0 m_e^2 \omega^2} \sum_i \int_{BZ} \frac{d\tilde{\mathbf{k}}}{(2\pi)^2} f(\tilde{\mathbf{k}}) |P_{\theta}^{\pm}(\tilde{\mathbf{k}})|^2 \\ & \times \delta [E_c(\tilde{\mathbf{k}}) - E_v(\tilde{\mathbf{k}}) - \omega], \end{aligned} \quad (21)$$

where $E_c(\tilde{\mathbf{k}})$ and $E_v(\tilde{\mathbf{k}})$ are the energies of the conduction and valence bands and $f(\tilde{\mathbf{k}})$ is the Fermi distribution function. By adjusting the energy of light to the band edge, $\omega = E_c(\tilde{\mathbf{k}}) - E_v(\tilde{\mathbf{k}}) = 2|\tilde{m}|$, we find

$$\varepsilon_{\pm}(\omega = 2|\tilde{m}|) = \frac{\pi e^2}{4\varepsilon_0 m_e^2 \tilde{m}^2} |P_{\theta}^{\pm}(0)|^2, \quad (22)$$

which means that $|P_{\theta}^{\pm}(0)|^2$ can be directly observed by optical absorption. It is possible to excite electrons selectively at the Λ_X (Λ'_X) or Λ_Y (Λ'_Y) point by setting $\theta = \theta_c$ for $c = 1, 2, 3, 4$.

We have studied analytically the optical matrix element $|P_{\theta}^{\pm}(\tilde{\mathbf{k}})|$ at the Λ_X (Λ'_X) point. Next we investigate it away from the Λ_X (Λ'_X) point. We show the optical matrix element of right and left elliptically polarized light $|P_{\theta_c}^{\pm}(\tilde{\mathbf{k}})|^2$ calculated numerically from the Hamiltonian (1) in Fig.4. There are sharp peaks in optical absorption near the Λ_X (Λ'_X) points. Fig.4(a) shows the optical matrix element $|P_{\theta_c}^+(\tilde{\mathbf{k}})|^2$ and $|P_{\theta_c}^-(\tilde{\mathbf{k}})|^2$ along the \tilde{k}_y axis. We clearly see the difference between the right and left polarized lights at the Λ_X (Λ'_X) point. There is large optical absorption in right polarized light, while no optical absorption in left polarized light. This is a dichroism caused by elliptically polarized light, and the key feature of the elliptic dichroism.

The k -resolved optical polarization $\eta(\tilde{\mathbf{k}})$ is given by⁴⁻⁷

$$\eta(\tilde{\mathbf{k}}) = \frac{|P_{\theta_c}^+(\tilde{\mathbf{k}})|^2 - |P_{\theta_c}^-(\tilde{\mathbf{k}})|^2}{|P_{\theta_c}^+(\tilde{\mathbf{k}})|^2 + |P_{\theta_c}^-(\tilde{\mathbf{k}})|^2}, \quad (23)$$

which we show in Fig.4(b). This quantity is the difference between the absorption of the left- and right-handed lights (\pm),

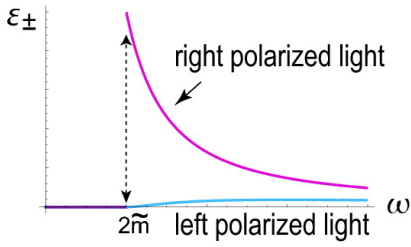


FIG. 5: (Color online) Imaginary part of dielectric function $\varepsilon_{\pm}(\omega)$ due to interband absorptions at $\theta = \theta_1$. [eq.(29)]. A clear difference is observed between the right and left polarized lights. There is almost no optical absorption for left polarized light for $\omega > 2\tilde{m}$.

normalized by the total absorption, around the Λ point. Optical polarizations are perfectly polarized at the Λ_X and Λ'_X points ($\tilde{\mathbf{k}} = 0$). Namely, the selection rule holds exactly at the Λ_X and Λ'_X points. Then, $|\eta(\tilde{\mathbf{k}})|$ rapidly decreases to 0 as $|\tilde{\mathbf{k}}|$ increases.

We proceed to drive the analytic expression of $|P_{\theta}^{\pm}(\tilde{\mathbf{k}})|$ away from the Λ_X and Λ'_X points with the use of the low-energy Hamiltonian (6) in (14). It is straightforward to find that

$$P_x(\tilde{\mathbf{k}}) = v_1 \frac{v_1 \tilde{k}_x \tilde{m} + i \tilde{v}_2 \tilde{k}_y \sqrt{\tilde{m}^2 + \tilde{v}_1^2 \tilde{k}_x^2 + \tilde{v}_2^2 \tilde{k}_y^2}}{\sqrt{\tilde{v}_1^2 \tilde{k}_x^2 + \tilde{v}_2^2 \tilde{k}_y^2} \sqrt{\tilde{m}^2 + \tilde{v}_1^2 \tilde{k}_x^2 + \tilde{v}_2^2 \tilde{k}_y^2}}, \quad (24)$$

$$P_y(\tilde{\mathbf{k}}) = \tilde{v}_2 \frac{\tilde{v}_2 \tilde{k}_y \tilde{m} - i v_1 \tilde{k}_x \sqrt{\tilde{m}^2 + \tilde{v}_1^2 \tilde{k}_x^2 + \tilde{v}_2^2 \tilde{k}_y^2}}{\sqrt{\tilde{v}_1^2 \tilde{k}_x^2 + \tilde{v}_2^2 \tilde{k}_y^2} \sqrt{\tilde{m}^2 + \tilde{v}_1^2 \tilde{k}_x^2 + \tilde{v}_2^2 \tilde{k}_y^2}}, \quad (25)$$

since $\mathcal{P}_x = v_1 \sigma_x$ and $\mathcal{P}_y = \tilde{v}_2 \sigma_y$. In the case of $\theta = \theta_1$, it yields a simple form,

$$|P_{\theta_1}^{\pm}(\tilde{\mathbf{k}})|^2 = m_0^2 v_1 \tilde{v}_2 \frac{\left(\pm \tilde{m} + \sqrt{\tilde{m}^2 + \tilde{v}_1^2 \tilde{k}_x^2 + \tilde{v}_2^2 \tilde{k}_y^2} \right)^2}{\tilde{m}^2 + \tilde{v}_1^2 \tilde{k}_x^2 + \tilde{v}_2^2 \tilde{k}_y^2}. \quad (26)$$

Using the fact $\varepsilon_v(\tilde{\mathbf{k}}) = -\varepsilon_c(\tilde{\mathbf{k}})$ and representing (26) in terms of the energy (9), we obtain

$$|P_{\theta_1}^{\pm}(\tilde{\mathbf{k}})|^2 = m_0^2 v_1 \tilde{v}_2 \frac{(\pm \tilde{m} + E_v(\tilde{\mathbf{k}}))^2}{[E_v(\tilde{\mathbf{k}})]^2}. \quad (27)$$

We substitute (27) to (21), and use the density of state

$$\rho(E) = \frac{|E|}{2\pi v_1 \tilde{v}_2} \Theta(E - 2\tilde{m}) \quad (28)$$

with the step function $\Theta(x) = 1$ for $x > 0$ and $\Theta(x) = 0$ for $x < 0$, to find

$$\varepsilon_{\pm}(\omega) = \frac{e^2 m_0^2}{2\varepsilon_0 m_e^2 \omega} \frac{(\pm \tilde{m} + \omega/2)^2}{(\hbar\omega/2)^2} \Theta(\omega - 2\tilde{m}). \quad (29)$$

There is no optical absorption for left polarized light at the band gap

$$\varepsilon_{-}(\omega = 2\tilde{m}) = 0. \quad (30)$$

We show the optical absorption (29) in Fig.5. A clear difference is observed between the right- and left- polarized lights. There is almost no optical absorption for left polarized light for $\omega > 2\tilde{m}$.

V. CONCLUSION

We have investigated the optical absorption in the TCI surface. By measuring the ellipticity angle θ_1 of the injected beam at which the optical absorption vanishes, we can determine the anisotropy of the velocities of Dirac cones v_1/\tilde{v}_2 based on the formula $v_1/\tilde{v}_2 = \tan\theta_1$: See Fig.3. We can also determine the band gap by measuring the energy where the optical absorption becomes nonzero (29): See Fig.5. This method will be more precise to determine the anisotropy and the band gap of the Dirac cones than the ARPES.

The role of the right- and left-polarized light is inverted when the sign of the mass term is negative. Thus we can determine the sign of the mass term by the elliptic dichroism even when the magnitude of the mass term is very small.

An interesting valleytronics application of the elliptic dichroism would read as follows. Let us adjust the ellipticity of light at $\theta = \theta_1$ so that the optical absorption near the Λ_X point does not occur [Fig3](b1). Then the optical absorption is not zero at the Λ_Y point. Namely, we can selectively excite electrons at the Λ_Y point by left polarized light. It is a valley-selective optical pumping. In the same way, by adjusting $\theta = \theta_2$, we can selectively excite electrons at the Λ_X point by left polarized light. The valley-selective optical pumping is possible since the anisotropy of Dirac cones at Λ_X and Λ_Y points are different. If the Dirac cones were isotropic, we could not differentiate the Dirac cones at Λ_X and Λ_Y points since they have the same chirality. This will pave a new way to valleytronics in the TCI.

I am very much grateful to N. Nagaosa, Y. Ando, L. Fu and T. H. Hsieh for many helpful discussions on the subject. This work was supported in part by Grants-in-Aid for Scientific Research from the Ministry of Education, Science, Sports and Culture No. 22740196.

¹ A. Rycerz, J. Tworzydło, and C. W. J. Beenakker, Nat. Phys. **3**, 172 (2007).

² D. Xiao, W. Yao, and Q. Niu, Phys. Rev. Lett. **99**, 236809 (2007).

³ A. R. Akhmerov, C. W. J. Beenakker, Phys. Rev. Lett. **98**, 157003

(2007)

⁴ W. Yao, D. Xiao, and Q. Niu, Phys. Rev. B **77**, 235406 (2008).

⁵ D. Xiao, G.-B. Liu, W. Feng, X. Xu, and W. Yao, Phys. Rev. Lett. **108**, 196802 (2012).

- ⁶ X. Li, T. Cao, Q. Niu, J. Shi, and J Feng, PNAS 110 (10) 3738 (2013)
- ⁷ M. Ezawa, Phys. Rev. B 86, 161407(R) (2012)
- ⁸ M. Ezawa, Phys. Rev. B 87, 155415 (2013)
- ⁹ K. F. Mak, C. Lee, J. Hone, J. Shan, and T. F. Heinz, Phys. Rev. Lett. **105**, 136805 (2010)
- ¹⁰ A. Splendiani, L. Sun, Y. Zhang, T. Li, J. Kim, C.-Y. Chim, G. Galli, and F. Wang, Nano Lett. **10**, 1271 (2010)
- ¹¹ H. Zeng, J. Dai, W. Yao, D. Xiao and X. Cui, Nat. Nanotech. **7**, 490 (2012).
- ¹² T. Cao, G. Wang, W. Han, H. Ye, C. Zhu, J. Shi, Q. Niu, P. Tan, E. Wang, B. Liu and J Feng Nat. Com. **3**, 887 (2012).
- ¹³ K. F. Mak, K. He, J. Shan and T. F. Heinz, Nat. Nanotech. **7**, 494 (2012)
- ¹⁴ S. Wu, J. Ross, G. Liu, G. Aivazian, A. Jones, Z. Fei, W. Zhu, D. Xiao, W. Yao, D. Cobden, X. Xu, Nature Physics **9**, 149 (2013).
- ¹⁵ Y. Tanaka, Z. Ren, T. Sato, K. Nakayama, S. Souma, T. Takahashi, K. Segawa and Y. Ando, Nat. Phys. **8**, 800 (2012)
- ¹⁶ Su-Yang Xu, Chang Li, N. Alidoust, M. Neupane, D. Qian, I. Belopolski, J.D. Denlinger, Y.J. Wang, H. Lin, L.A. Wray, G. Landolt, B. Slomski, J.H. Dil, A. Marcinkova, E. Morosan, Q. Gibson, R. Sankar, F.C. Chou, R. J. Cava, A. Bansil and M.Z. Hasan, Nat. Com. **3**, 1192 (2012)
- ¹⁷ P. Dziawa, B. J. Kowalski, K. Dybko, R. Buczko, A. Szczerbakow, M. Szot, E. Lusakowska, T. Balasubramanian, B. M. Wojek, M. H. Berntsen, O. Tjernberg and T. Story, Nat. Mat. **11**, 1023 (2012).
- ¹⁸ L. Fu, Phys. Rev. Lett. **106**, 106802 (2011)
- ¹⁹ T. H. Hsieh, H. Lin, J. Liu, W. Duan, A. Bansil and L. Fu, Nat. Comm. **3**, 982 (2012).
- ²⁰ Y. Okada, M. Serbyn, H. Lin, D. Walkup, W. Zhou, C. Dhital, M. Neupane, S. Xu, Y. J. Wang, R. Sankar, F. Chou, A. Bansil, M. Z. Hasan, S. D. Wilson, L. Fu, V. Madhavan, Science **341** 1496 (2013).
- ²¹ J. Liu, W. Duan, L. Fu, Phys. Rev. B **88**, 241303(R) (2013)
- ²² C. Fang, M. J. Gilbert, S.-Y. Xu, B. A. Bernevig, and M. Z. Hasan, Phys. Rev. B **88**, 125141 (2013)
- ²³ J. Liu, T. H. Hsieh, P. Wei, W. Duan, J. Moodera and L. Fu, cond-mat/arXiv:1310.1044
- ²⁴ Y. J. Wang, W.-F. Tsai, H. Lin, S.-Y. Xu, M. Neupane, M. Z. Hasan, and A. Bansil, Phys. Rev. B **87** 235317 (2013)
- ²⁵ C. Fang, M. J. Gilbert, B. A. Bernevig, cond-mat/arXiv:1306.0888
- ²⁶ B. M. Wojek, R. Buczko, S. Safaei, P. Dziawa, J. Kowalski, M. H. Berntsen, T. Balasubramanian, M. Leandersson, Phys. Rev. B **87** 115106 (2013).
- ²⁷ S. Safaei, P. Kacman, and R. Buczko, Phys. Rev. B **88** 045305 (2013)